

# Beyond Ground: Map-Free LiDAR Relocalization for UAVs

Hengyu Mu<sup>1,2,\*</sup>, Jianshi Wu<sup>1,2,\*</sup>, Yuxin Guo<sup>1,2,\*</sup>, XianLian Lin<sup>1,2</sup>, Qingyong Hu<sup>3</sup>,  
Sheng Ao<sup>1,2</sup>, Chenglu Wen<sup>1,2</sup>, Cheng Wang<sup>1,2</sup>

<sup>1</sup> Fujian Key Laboratory of Sensing and Computing for Smart Cities, Xiamen University

<sup>2</sup> Key Laboratory of Multimedia Trusted Perception and Efficient Computing,  
Ministry of Education of China, Xiamen University

<sup>3</sup> Department of Computer Science at the University of Oxford

{23020250157845, wujianshi, guoyuxin}@stu.xmu.edu.cn, lxl@xmu.edu.cn,  
huqingyong15@outlook.com, {aosh, clwen, cwang}@xmu.edu.cn

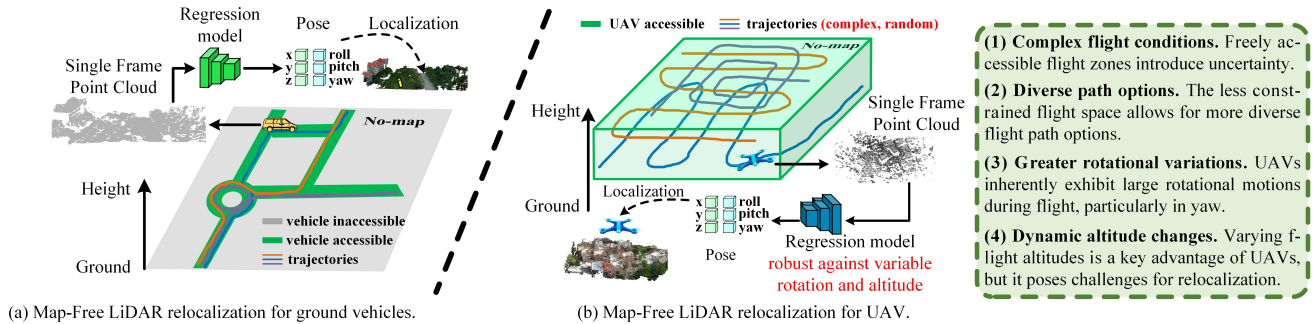


Figure 1. **The challenges of UAV’s map-free relocalization compared to vehicle.** This paper primarily investigates the map-free UAV relocalization. Compared to map-free vehicle relocalization, UAV relocalization faces greater challenges due to more complex and diverse flight conditions. Thus, developing a robust and accurate algorithm for UAV relocalization is urgently needed.

## Abstract

Localization is a fundamental capability in unmanned aerial vehicle (UAV) systems. Map-free LiDAR relocalization offers an effective solution for achieving high-precision positioning in environments with weak or unavailable GNSS signals. However, existing LiDAR relocalization methods are primarily tailored to autonomous driving, exhibiting significantly degraded accuracy in UAV scenarios. In this paper, we propose *MAILS*, a novel **map-free LiDAR relocalization framework for UAVs**. A *Locality-Preserving Sliding Window Attention* module is first introduced to extract locally discriminative geometric features from sparse point clouds. To handle substantial yaw rotations and altitude variations encountered during UAV flight, we then design a *coordinate-independent feature initialization module* and a *locally invariant positional encoding mechanism*, which together significantly enhance the robustness of fea-

ture extraction. Furthermore, existing LiDAR-based relocalization datasets fail to capture real-world UAV flight characteristics, such as irregular trajectories and varying altitudes. To address this gap, we construct a large-scale LiDAR localization dataset for UAVs, which comprises four scenes and various flight trajectories, designed to evaluate UAV relocalization performance under realistic conditions. Extensive experiments demonstrate that our method achieves satisfactory localization precision and consistently outperforms existing techniques by a significant margin. Our code and dataset will be released soon.

## 1. Introduction

Recently, Unmanned Aerial Vehicles have emerged as key enablers of the low-altitude economy [12, 54], supporting a wide range of applications such as terrain exploration, urban infrastructure inspection, and emergency response [14, 35, 54]. During UAV operations, accurate real-

\*Equal contribution.

time localization is essential for reliable mission execution. Most existing systems rely on GNSS signals [64] to determine the location of UAV. However, GNSS signals can be easily obstructed in urban environments or become entirely unavailable. Therefore, it is crucial to develop efficient and robust localization methods for UAVs.

Benefiting from LiDAR’s robustness to environmental interference and illumination changes [9, 33, 40], LiDAR-based localization provides a promising alternative to address the aforementioned problem [50, 55, 60, 66]. Several studies have explored LiDAR odometry [11, 39, 48] for UAV localization [19, 44, 61, 65]. However, these methods inevitably accumulate drift over time, resulting in progressively increased localization errors. Consequently, LiDAR odometry-based approaches face inherent limitations for long-term localization in real-world UAV applications [26, 38].

With advances in sensor technology, acquiring large-scale, high-precision LiDAR maps has become relatively straightforward. As a result, plenty of methods focus on 6-degrees-of-freedom (6-DoF) relocalization [1, 2, 8, 22, 56]. Despite achieving promising performance, these methods require expensive 3D map storage and incur high communication overhead [3, 7, 36, 39], which poses severe challenges for resource-constrained platforms such as UAVs [60]. This motivates the development of highly accurate, map-free [4] LiDAR relocalization approaches. In autonomous driving [63], a handful of methods have explored map-free LiDAR relocalization [29, 32, 57, 59]. They train deep neural networks to memorize spatial representations of scenarios, and directly regress the global pose for each input LiDAR scan during inference. Unfortunately, such methods cannot be directly applied to drone platforms. As illustrated in Fig. 1, unlike ground vehicles, UAVs operate under (1) more complex flight conditions, (2) more diverse path options, (3) greater rotational variations (especially in yaw direction), and (4) more dynamic altitude changes, which together introduce new challenges.

To address the aforementioned challenges, we design a new LiDAR relocalization framework for UAV, which can effectively learn locally discriminative geometric features. To ensure robustness under diverse UAV flight conditions, the proposed model satisfies three key properties: 1) Rotation invariance in azimuth. The model remains unaffected by frequent and large yaw rotations that commonly occur during UAV flight. 2) Altitude robustness. For LiDAR scan captured at varying altitudes in the same location, the model encodes them into similar feature representations, thereby mitigating the influence of altitude variations. 3) Local descriptiveness. Since UAV trajectories often yield point clouds with partial overlap, the model must exhibit strong discriminative capability for local geometric features to handle complex and irregular flight paths.

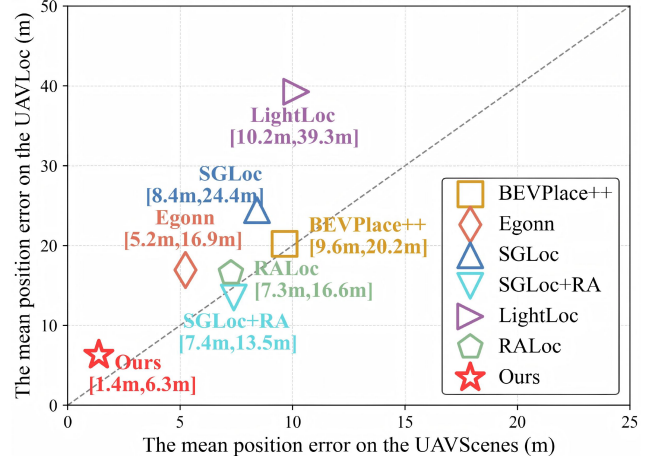


Figure 2. Mean position errors of different methods on the UAVScenes and UAVLoc (ours) datasets. Our method achieves the best performance on both datasets.

Specifically, we propose MAILS, a map-free LiDAR relocalization framework designed to achieve high-accuracy and robust pose estimation in low-altitude flight scenarios. To handle large azimuthal variations and substantial altitude changes, we introduce the Locality-Preserving Sliding Window Attention (LoSWAtt) module to extract locally discriminative geometric features. Furthermore, to mitigate feature degradation under large rotational motions, LoSWAtt incorporates a yaw- and altitude-invariant positional encoding, enabling robust feature extraction across varying orientations and heights. Finally, to evaluate relocalization performance in real-world conditions, we build a LiDAR-equipped drone platform and collect a large-scale outdoor dataset for LiDAR relocalization, featuring irregular flight paths and diverse altitudes. As shown in Fig. 2, our method achieves state-of-the-art performance on two challenging drone datasets.

Overall, our contributions are summarized as follows:

- We conduct the first systematic study of map-free LiDAR relocalization for UAVs, analyze the unique challenges in this setting, and provide a tailored solution.
- We propose a new LiDAR relocalization framework that extracts discriminative geometric features and improves robustness to azimuthal and altitude changes.
- We collect a large-scale LiDAR localization dataset with diverse flight trajectories and altitude variations, providing a challenging benchmark for future research.
- We perform extensive experiments and ablation studies, demonstrating the efficacy of our method and offering insights into the design choices behind it.

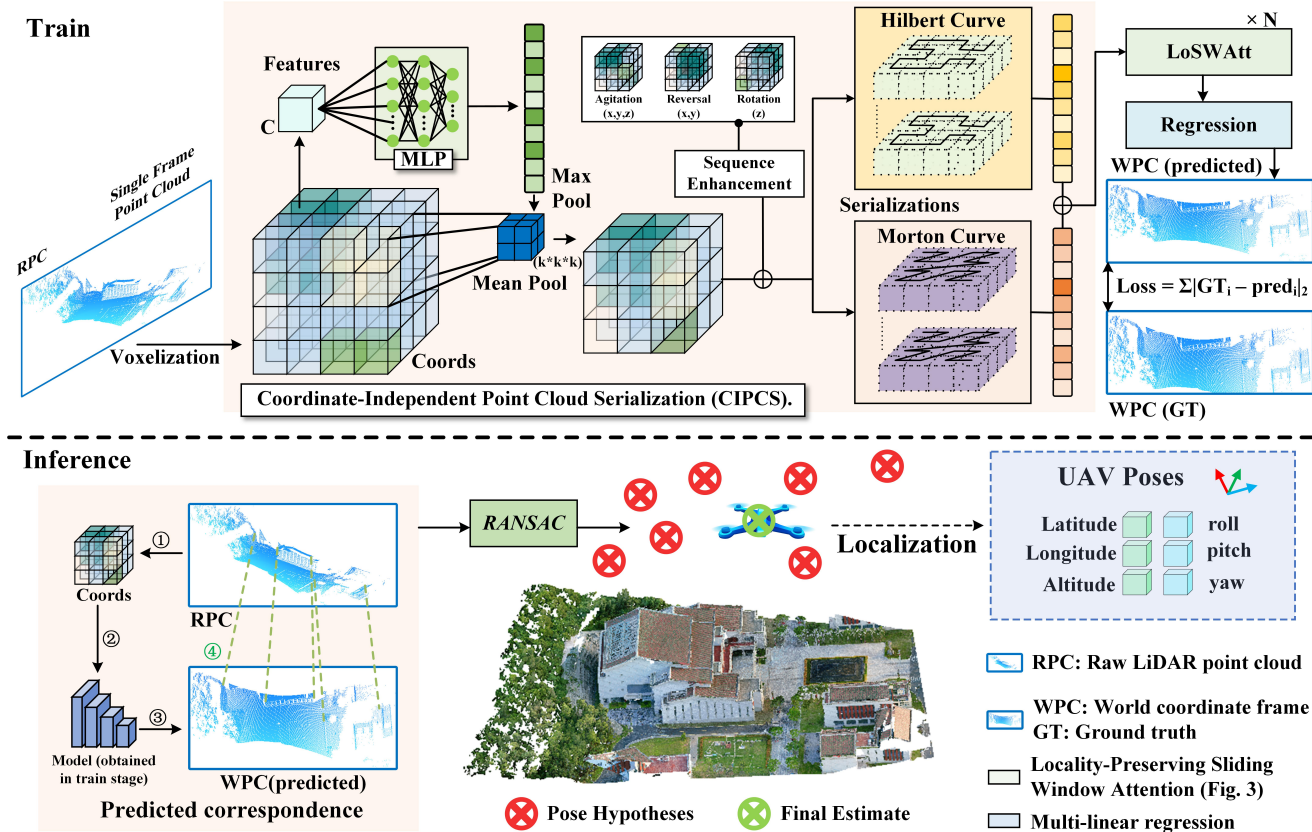


Figure 3. **The pipeline of MAILS.** MAILS consists of two main components:(1) Raw coordinate-independent point cloud serialization initializes point cloud features to a serialization. (2) The Locality-preserving Sliding Window Attention module encodes robust point cloud features (detailed in Fig. 4). RANSAC is used to 6-DoF pose estimation in inference stage.

## 2. Related work

### 2.1. Conventional Relocalization

Conventional relocalization methods[31, 58, 67] aim to align the query point cloud with a pre-constructed 3D map. These approaches are typically categorized into two main types: retrieval-based methods [24, 47, 56] and matching-based methods [41]. Retrieval-based methods treat relocalization as a task of recognizing a place. To do this, they need a pre-built database of feature descriptors and use similarity queries to find the point cloud that is most like the one they are looking for [62]. On the other hand, matching-based methods look for frames that are similar in a global descriptor database or a 3D map. Then, they match the features of the query frame to those of the reference map [34]. However, both types inherently rely on pre-built maps, leading to challenges in data storage and communication efficiency.

### 2.2. Regression-based Localization

Recently, deep learning-based relocalization methods[20, 21, 30, 42] have achieved remarkable progress by formulating the task as a regression problem, thereby enabling direct

end-to-end prediction of 6-DoF poses. Specifically, Point-Loc [52] pioneered a LiDAR-based Absolute Pose Regression (APR) framework, realizing map-free relocalization for ground vehicles. Subsequently, HypLiLoc [49] leveraged multi-level feature representations to capture more discriminative scene features. DiffLoc [28] improved accuracy by transforming pose regression process into multi-iterative steps through the diffusion model [13, 18].

However, as noted in [27], APR methods primarily emphasize high-dimensional pose–feature mappings, which constrains their relocalization accuracy—particularly in large-scale outdoor environments [59]. To overcome this limitation, Scene Coordinate Regression (SCR) methods[17, 45] were introduced, which predicts the world-coordinate position of each point, and subsequently employ RANSAC to estimate the final 6-DoF pose. Specifically, SGLoc [27] was the first to integrate the SCR framework into LiDAR-based localization. Subsequently, LiSA [57] incorporated semantic information to reduce the influence of noisy or disruptive points within the scene, further improving localization accuracy. More recently, RALoc [59]

has focused on mitigating rotation-related challenges during the pose estimation process. These SCR methods work well for vehicle-based LiDAR localization, but they don't work as well for UAV-based LiDAR localization. This degradation arises from the complex flight conditions. Therefore, we aim to address the challenging of UAV relocalization.

### 3. Method

As previously mentioned, SCR-based methods have demonstrated strong performance on ground-vehicle datasets [27, 59]. However, as illustrated in Fig. 1, UAVs exhibit more complex flight trajectories, larger azimuthal changes, and greater altitude variations than ground vehicles, which significantly degrade the performance of localization techniques tailored to autonomous driving.

To address this issue, we propose MAILS, which learns yaw- and altitude-invariant point cloud features through a feature encoder that is more robust to local geometric variations. Moreover, to evaluate performance under realistic flight conditions and alleviate the limitations of existing benchmarks, we collect UAVLoc, a large-scale UAV LiDAR dataset with random trajectories and substantial altitude variations within each scene.

#### 3.1. MAILS

**Framework.** Similar to SCR-based vehicle relocalization methods [27], we define the overall MAILS framework as follows. Given a query point cloud  $P_t \in \mathbb{R}^{N \times 3}$ , our objective is to estimate the UAV's global 6-DoF pose  $p$ . As illustrated in Figure 3, MAILS first learns to regress point-wise correspondences from the raw point cloud to predict its world coordinates  $Y$ . Specifically, this mapping is realized by a learnable model  $F$ , such that

$$Y = \mathcal{F}(P_t). \quad (1)$$

During inference, we leverage the predicted correspondences  $(P_t, Y)$  to estimate the pose. We employ RANSAC[15, 43] to robustly sample  $M$  candidate correspondence sets and solve for the transformation that minimizes the following energy function:

$$p^* = \arg \min_{T_p} \sum_{i=1}^M \left\| T_p p_t^{(i)} - \mathbf{y}^{(i)} \right\|_2, \quad (2)$$

where  $T_p$  is a  $4 \times 4$  matrix representation of the pose  $p$ ,  $i$  is the index of the point,  $p_t^{(i)}$  is a point in  $P_t$ , and  $\mathbf{y}^{(i)}$  is its corresponding predicted global coordinate in  $Y$ .

Specifically, as illustrated in Fig. 3, MAILS is divided into two main components: (1) Coordinate-Independent Point Cloud Serialization (CIPCS), which initializes point cloud features through a serialization process that is independent of their original coordinates (XYZ). (2) Locality-Preserving Sliding Window Attention (LoSWAtt) module,

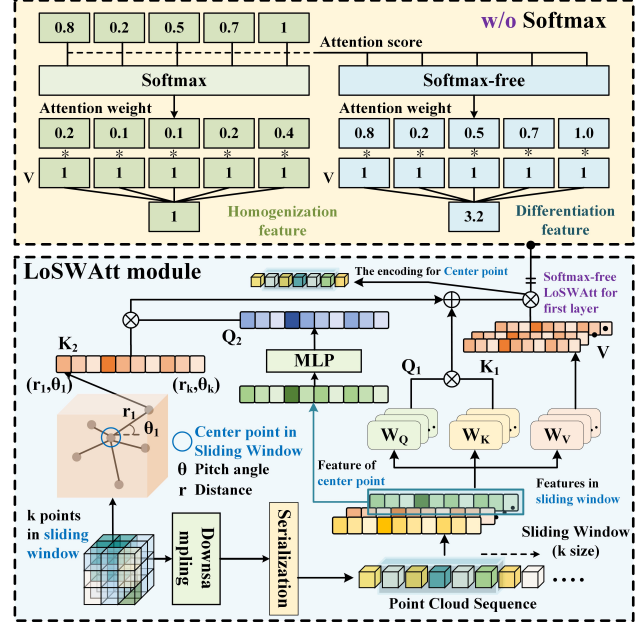


Figure 4. Locality-Preserving Sliding Window Attention module. This module is designed to encode local geometric features. Notably, the first layer of the LoSWAtt module employs a Softmax-free design to produce differentiated features.

which employs a sliding-window local attention encoder together with yaw- and altitude-invariant positional encoding, enabling the encoding of features that remain robust to rotational and altitude variations.

**Coordinate-Independent Point Cloud Serialization.** To address the challenges posed by yaw and altitude changes in UAV, we designed a Coordinate-Independent Point Cloud Serialization (CIPCS) method, as shown in Fig. 3.

Due to the complex flight trajectories of UAVs, the relative XYZ coordinates of the same point cloud often undergo substantial and frequent variations. To address this, we replace the XYZ coordinates with a constant  $C$  as the raw feature for each point. The raw features are then expanded in dimension via an MLP (Multi-Layer Perceptron), followed by downsampling of both voxels and features to obtain the final point cloud feature  $F$ , which is shown in Eq. 3.

$$F = \text{Downsampling} \left( \left\{ \varphi(C) \right\}_{i=1}^N \right), \quad (3)$$

where  $N$  is the number of points,  $i$  is the index of the point,  $\varphi_1$  denotes multi-layer perceptron, and  $C$  is 1 in this paper. After that, we serialize the point cloud voxels using Hilbert and Morton curves which have been widely adopted in point cloud voxel serialization due to their strong locality-preserving properties [53].

**Locality-Preserving Sliding Window Attention.** To initialize and extract point cloud features with invariance to yaw rotations and altitude variations, we propose the

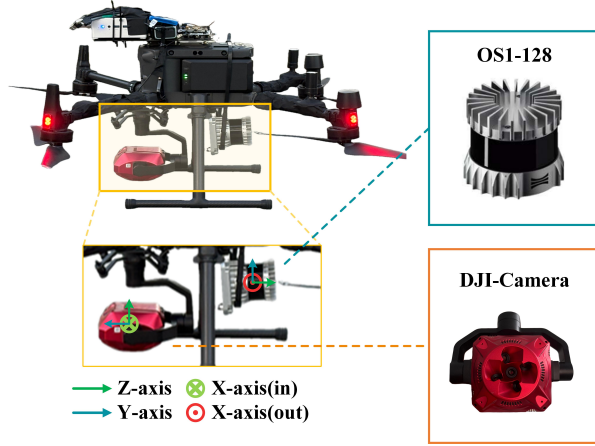


Figure 5. We scan point clouds and record GT using a UAV equipped with an Ouster OS1-128 LiDAR and a DJI-camera.

Locality-Preserving Sliding Window Attention (LoSWAtt) module, as illustrated in Fig. 4.

Specifically, we compute a local attention mechanism over the point cloud sequence using a sliding window of size  $k$ . This sliding window design not only enables the model to extract locally invariant geometric features but also effectively reduces the spatial complexity from  $O(n^2)$  to  $O((2k+1)n)$ . For the sliding window at step  $i$ , we define its local input feature  $F_i^w$  as:

$$F_i^w = \{\mathbf{f}_{i-k}, \mathbf{f}_{i-k+1}, \dots, \mathbf{f}_i, \dots, \mathbf{f}_{i+k}\} \quad (4)$$

Subsequently, we encode the  $F_i^w$  using an attention mechanism with a positional bias that preserves local invariance. The specific process is shown in Eq. 5.

$$\mathbf{f}'_i = \text{Softmax} \left( \frac{\mathbf{Q}\mathbf{K}^\top}{\sqrt{D}} + \frac{\mathbf{Q}_2\mathbf{K}_2^\top}{\sqrt{D_2}} \right) \mathbf{V}, \quad (5)$$

where  $D$  and  $D_2$  denote the dimensions of  $\mathbf{Q}$  and  $\mathbf{Q}_2$ , and  $\mathbf{Q}, \mathbf{K}, \mathbf{V} = P_{Q,K,V}(F_i^w)$ ,  $\mathbf{Q}_2 = \varphi_2(f_i)$ . Simultaneously, we compute the relative position  $r$  of each point within the sliding window relative to the central point, and use the pitch angle  $\theta$ , independent of yaw, as  $K_2$ , thereby providing the encoder with positional encoding that is invariant to both yaw and altitude variations, which is shown in Eq. 6

$$K_2 = \varphi_3 [(r_{i-k}, \theta_{i-k}), \dots, (r_{i+k}, \theta_{i+k})], \quad (6)$$

Finally, we obtain the predicted world coordinates  $Y'$  for each point through multiple linear regression heads.

**Softmax-free LoSWAtt.** Although the RCIPS eliminates the effects of XYZ rotation and translation, the resulting feature points across different point clouds are not distinctive, because the constant  $C$  is transformed into the same constant  $C_2$  through the  $\varphi$ . Consequently, these features

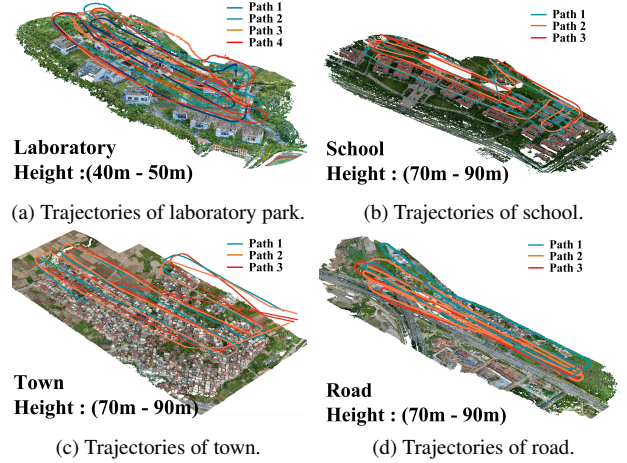


Figure 6. The flight paths of UAVLoc dataset.

cannot be directly used in the subsequent regression encoding stage. Therefore, we achieve distinctive point cloud features by designing the first-layer LoSWAtt module **without Softmax**, which is simple but necessary.

Specifically, as illustrated in the upper part of Fig. 4 (w/o Softmax), the point cloud feature  $F$  is treated as a constant  $C_2$  and thus remains constant after linear projection. Consequently,  $\mathbf{Q}, \mathbf{K}, \mathbf{Q}_2$ , and  $\mathbf{V}$  in Eq. 5 all collapse to constant vectors. Although  $\mathbf{K}_2$  introduces variation into the attention scores, the Softmax normalization suppresses these variations, leading to degraded attention expressiveness and resulting in highly homogeneous features. This phenomenon is clearly verified by the ablation results presented in Table 4, where we observed the performance of MAILS largely degrade when the first LoSWAtt module was without softmax-free. We obtain a distinctive local geometric encoding  $F'$  through the first LoSWAtt module, which is invariant to rotations and altitude variations.

**Loss function.** During training, the point cloud with global poses predicted by the network  $\mathcal{F}$  is optimized by  $\mathcal{L}_{L1}$ . Specifically, we minimize the average plain Euclidean distance between the predicted scene coordinates  $y_i$ , and the ground truth of scene coordinates  $y_i^*$ :

$$\mathcal{L}_{L1} = \frac{1}{|\mathbf{P}_t|} \sum_{y_i \in \mathbf{P}_t} \|y_i - y_i^*\|_1, \quad (7)$$

### 3.2. Dataset

UAV relocalization is substantially challenging due to significant rotational motions and complex flight trajectories. The existing UAVScenes[51] dataset provides UAV-mounted LiDAR data at fixed flight paths and altitudes, which fail to reflect real-world UAV scenarios where UAVs can vary their trajectory and altitude. To address this gap, we construct a LiDAR relocalization for UAV dataset,

Table 1. **Related Datasets.** LiDAR: Number of LiDAR sensors and LiDAR type. Scale: LiDAR coverage across all flight scenes. Trajectory: Flight path variation across different paths in the same scene. Variable altitude: Flight altitude variation across different paths in the same scene. Reloc: Whether the dataset can be used for relocalization tasks.

Dataset	Year	Domain	Platform	LiDAR	Scale	Trajectory	Variable altitude	Reloc
KITTI[16]	2013	Ground	Car	1 x VLP-64E	Large	Same	×	✓
NCLT[10]	2015	Ground	UGV	3 x 3D HDL-32E	Large	Same	×	✓
Oxford[5]	2016	Ground	Car	1 x SICK 3D	Large	Same	×	✓
NTU-VIRAL[38]	2021	Aerial	UAV	2 x Ous.-16	Small	Irregular	✓	–
UAVScenes[51]	2025	Aerial	UAV	1 x Livox Avia	Large	Same	×	✓
MUN-FRL[46]	2022	Aerial	Helicopter	1 x VLP-16	Large	Irregular	✓	×
<b>UAVLoc (ours)</b>	2025	Aerial	UAV	1 x Ous.-128	Large	Irregular	✓	✓

Table 2. **Results on UAVScenes dataset.** We report the mean error [m/°] for six methods on the UAVScenes datasets.

Method	Map-based Relocalization		Map-free Relocalization				
	BEVPlace++	Egonn	SGLoc	SGLoc+RA	LightLoc	RALoc	ours
HKairport	6.90m,5.37°	4.53m,4.19°	2.68m,2.57°	3.69m,2.30°	3.88m,4.13°	1.97m,2.24°	<b>1.06m,1.46°</b>
HKisland	5.19m,3.39°	3.78m,4.24°	6.83m,3.03°	6.85m,3.16°	6.95m,5.80°	1.81m,2.24°	<b>1.03m,1.85°</b>
AMtown	10.76m,6.77°	4.31m,4.20°	12.16m,7.56°	9.43m,5.24°	11.48m,7.65°	11.93m,7.11°	<b>1.34m,2.68°</b>
AMvalley	15.71m,7.92°	8.33m,4.57°	12.01m,5.00°	9.60m,7.75°	18.31m,8.39°	13.32m,5.37°	<b>2.14m,2.15°</b>
Average	9.64m,5.86°	5.24m,4.30°	8.42m,4.54°	7.39m,4.61°	10.16m,6.49°	7.26m,4.24°	<b>1.39m,2.04°</b>

UAVLoc, featuring extensive rotations, significant altitude variations, and irregular flight trajectories in each scene.

**Sensors setup.** As shown in Fig. 5, our dataset primarily comprises two sensors: (1) an Ouster OS1-128, a 128-beam spinning LiDAR used for point cloud acquisition, with its field of view (FOV), resolution, and frame rate (FPS) configured to  $[-22.5^\circ, 22.5^\circ]$ ,  $20 \times 1024$ , and 20 Hz, respectively. (2) A DJI camera directly records the UAV’s pose information and refines it through image-based optimization, yielding highly accurate UAV pose.

**Sensors calibration.** Following UAVScenes[51] and KITTI[16], we applied the Iterative Closest Point algorithm [6] to correct minor pose deviations caused by airflow turbulence during UAV flights. This process ensured accurate point cloud alignment and further facilitated precise extrinsic calibration between the LiDAR and DJI camera.

**Target environments.** Our dataset comprises flight data collected across four representative environments: a laboratory park, a school area, a town and a road area. These environments exhibit diverse structural characteristics and expansive fields of view. Furthermore, non-repetitive flight paths were performed in each environment to evaluate relocalization performance under realistic and unconstrained flight conditions, which are shown in Fig. 6.

Additionally, to capture altitude variations during UAV operation, we collected at least one flight trajectories with varying altitudes in each scene. This enables the evaluation of relocalization robustness under altitude-varying conditions. Notably, such irregular flight paths and alti-

tude changes pose substantial challenges for relocalization, while more faithfully reflecting UAVs’ flight conditions.

**Collection divisions of UAVLoc.** The dataset consists of 4 scenarios divided into UAVLoc\_C (Common Collection, including the laboratory area) and UAVLoc\_U (Challenges Collection, including other three scenarios). For UAVLoc\_C, we collected 4 flight paths at altitudes of 40m, 40m, 45m, and 50m along non-fixed routes in the laboratory area. This collection enables the assessment of UAV relocalization performance in real-world operational scenarios. For UAVLoc\_U, we collected 9 flight paths at altitudes over 70m along non-fixed routes in three different areas. Given that the UAV operated near the maximum LiDAR range, the point clouds were highly sparse and limited in field of view. Consequently, there was minimal overlap between trajectories, providing a challenging dataset for assessing relocalization methods under extreme conditions.

**Comparison with other datasets.** Table 1 provides a comparison between our dataset and other existing datasets, including UAVScenes[51], NTU-VIRAL[38], MUN-FRL[46], KITTI[16], NCLT[10], and Oxford[5]. Our goal is to design and validate robust and accurate UAV relocalization algorithms by collecting a dataset with irregular flight paths and varying altitudes. Overall, our dataset highlights the following key characteristics: 1) Multiple flight paths. 2) Irregular flight paths. 3) Altitude variation. More details about our dataset please see the appendix.

Table 3. **Results on UAVLoc dataset.** We report the mean error [m/°] for six methods on the UAVLoc datasets.

Method	Map-based Relocalization		Map-free Relocalization				
	BEVPlace++	Egonn	SGLoc	SGLoc+RA	LightLoc	RALoc	ours
Laboratory_3	25.35m,11.59°	15.95m,10.76°	24.78m,14.78°	12.47m,10.46°	39.85m,20.34°	22.13m,13.67°	<b>6.69m,1.75°</b>
Laboratory_4	15.10m,11.47°	17.92m,14.37°	24.07m,17.52°	14.51m,10.73°	38.68m,28.19°	11.02m,9.17°	<b>5.89m,1.75°</b>
Average	20.23m,11.53°	16.94m,12.57°	24.43m,16.15°	13.49m,10.60°	39.26m,24.27°	16.57m,11.42°	<b>6.29m,1.75°</b>

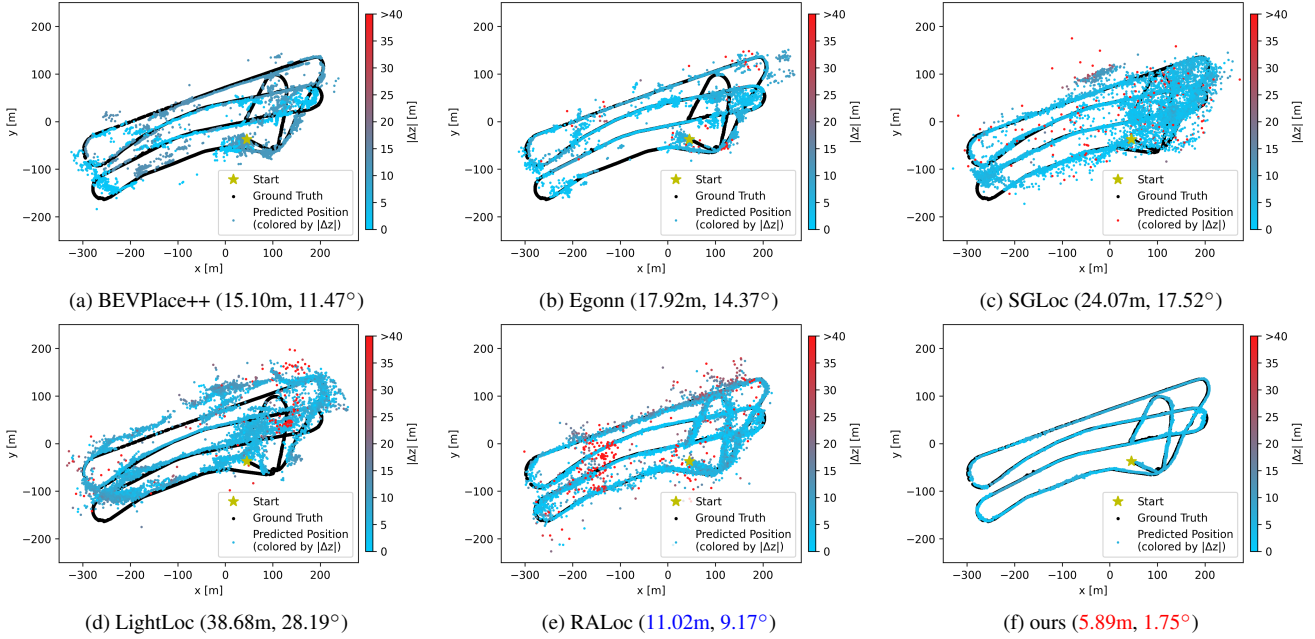


Figure 7. Localization results of different methods on the UAVLoc dataset (Laboratory\_4). We highlight the **best** and **second-best** results.

## 4. Experiment

### 4.1. Setup

**Datasets and metrics.** We evaluate MAILES on two large-scale outdoor UAV-LiDAR datasets, namely UAVScenes[51] and our proposed UAVLoc dataset. In this section, we report two evaluation metrics: the mean position error and the mean orientation error.

**UAVScenes.** UAVScenes dataset[51], which built upon the MARS-LVIG dataset[26], was a critical benchmark for UAV relocalization. This dataset contains LiDAR and camera recordings collected across four representative large-scale scenes (towns, valleys, airports, and islands) and provides accurate 6-DoF poses. For each scene, multiple flights were conducted along identical paths, making it particularly suitable for benchmarking UAV relocalization methods. In our experiments, we use the first two flights of each scene for training and the final flight for testing.

**UAVLoc.** We construct UAVLoc, a large-scale outdoor UAV-LiDAR relocalization dataset covering four representative scenes, including the laboratory park, the school, the town, and the road, where each scene spans approximately

1.3  $km^2$  on average. The dataset contains two collections, including UAVLoc\_C and UAVLoc\_U. In this paper, to validate UAV relocalization performance under real-world conditions, we primarily present and analyze results on UAVLoc\_C. Our approach also demonstrates significantly superior performance on UAVLoc\_U over other methods. Comprehensive results on UAVLoc\_U are included in the supplementary. On UAVLoc\_C, the first two trajectories are used for training, and other two for testing.

**Implementation.** Our method is implemented by Pytorch. We conduct our experiments on a server equipped with an Intel Xeon(R) Gold 6342 CPU, and one NVIDIA RTX 5090 GPUs. During training, we use the Adam optimizer[23] with a learning rate of 0.002 and a batch size of 120.

**Baseline.** As this work represents the first study on LiDAR-based map-free UAV relocalization, we select several representative and competitive baseline methods, which are among the most advanced approaches in vehicle-LiDAR relocalization, to comprehensively evaluate the performance of our model. Specifically, for SCR-based methods, we consider SGLoc [27], LightLoc [29], and RALoc [59] as baseline methods. For SGLoc, rotation augmentation was

Table 4. **Results of Ablation Study.** The results on UAVScenes and UAVLoc, where w/o means without, and R/ means Replacing.

Modules	AMvalley (UAVScenes)	Laboratory_3 (UAVLoc)	Laboratory_4 (UAVLoc)
(1) R/ constant features	5.84m,4.46°	32.94m,21.28°	13.79m,9.50°
(2) w/o Softmax	262.33m,123.67°	186.02m,125.42°	179.65m,125.02°
(3) R/ LoSWAtt	143.33m,71.12°	154.67m,74.69°	182.44m,82.35°
(4) w/o Position Encoding	230.78m,120.77°	178.87m,122.26°	168.76m,123.99°
(5) <b>The Full Method</b>	<b>2.14m,2.15°</b>	<b>6.69m,1.75°</b>	<b>5.89m,1.75°</b>

not originally applied, unlike other methods designed to handle rotation. To ensure experimental fairness, we additionally report the results of SGLoc with rotation augmentation, denoted as SGLoc+RA. Additionally, to further validate the effectiveness of our proposed method, we compare it against advanced conventional relocalization methods for vehicle, including BEVPlace++[37] and Eggon[25].

## 4.2. Results

### 4.2.1. Comparison with other methods

**Result on UAVScenes:** Table 2 reports the comparison between our approach and existing methods on the UAVScenes dataset. Our method achieves state-of-the-art performance, yielding an average position error of 1.39 m and an average orientation error of 2.04° across four validation scenes. These results substantially surpass those of the comparison methods. Vehicle relocalization methods shows accuracy diminishes notably in UAV scenarios. Compared with SGLoc, our method reduces the mean position error by 7.03 m and the mean orientation error by 2.5°, respectively. Although applying rotation augmentation slightly improved SGLoc performance on the AMtown and AMvalley tracks, it caused a noticeable decline in accuracy on HKairport (2.68 m to 3.69 m). This suggests that data augmentation alone is insufficient to handle the complex and diverse UAV poses, whereas our rotation-invariant feature encoding provides a more robust and generalizable solution. LightLoc exhibited relatively poor performance because it relies on the feature extractor, which is designed for ground vehicle. RALoc achieves great performance, primarily due to its strong robustness to rotational disturbances. Our method achieves state-of-the-art performance by effectively addressing UAV-specific relocalization challenges, particularly the variations in yaw and altitude.

**Result on UAVLoc:** As previously mentioned, the results on UAVScenes are difficult to comprehensively evaluate for UAV relocalization methods. Therefore, we collected a more realistic UAV dataset, UAVLoc, for validation. In Table 3, we demonstrate the Comparison of our method and other methods on proposed UAVLoc. The results indicate that irregular flight trajectories and UAV poses pose significant challenges for all relocalization methods. Except for our proposed method, all other methods exhibit average po-

sition errors exceeding 10 meters and average orientation errors over 10°. Although our method experienced a slight performance decline, it still achieves state-of-the-art performance, with average position errors by 6.29m and average orientation errors by 1.75°. This demonstrates that the proposed MAILS exhibits strong robustness against interference in UAV relocalization. Additionally, we visualized the relocalization results of all methods in Fig. 7 to provide a more intuitive comparison of their performance.

### 4.2.2. Ablation Study

To systematically evaluate the effectiveness of each component in MAILS, we conducted extensive model ablation experiments on UAVScenes (AMvalley) and UAVLoc (Laboratory). The results are shown in Tab. 4.

**(1) Only replacing constant raw features by XYZ.** We used a constant value as the raw point cloud feature to eliminate the effects of large UAV yaw rotations and altitude variations. In this experiment, we converted the raw features back to classical XYZ relative coordinates. The results indicate that, after this conversion, the features no longer remain invariant to rotations and altitude variations.

**(2) Only removing Softmax-free in first LoSWAtt.** In the first LoSWAtt module, we incorporate a Softmax-free module to generate distinguishable features and prevent the attention mechanism from collapsing. This design is critical and indispensable. The results show that removing this module leads to a complete failure of our method.

**(3) Only replacing the LoSWAtt by Point transformer [53].** LoSWAtt module adopts a local encoding that is invariant to yaw rotation and altitude changes. To assess its effectiveness, we replace the LoSWAtt with the classical Point Transformer v3. However, this replacement causes the model to lose its ability to encode locally invariant features, leading to a substantial decline of performance.

**(4) Only removing Position Encoding in LoSWAtt.** Position encoding plays a vital role in producing distinctive features and in encoding features that maintain local invariance. Our ablation results show that removing position encoding leads to the loss of this local invariance capability, thereby significantly weakening the robustness of the encoded features.

## 5. Conclusion

In this paper, we identify a critical gap in current research on map-free LiDAR relocalization and show that vehicle-based relocalization methods suffer substantial accuracy degradation when transferred to aerial scenarios. We propose MAILES, a new scene coordinate regression framework for UAV LiDAR relocalization that is highly robust to both azimuthal and altitude variations. To enable realistic evaluation and foster further progress in this area, we develop a UAV LiDAR system and collect a large-scale LiDAR localization dataset with random flight trajectories and altitude changes. Extensive experiments demonstrate that our MAILES consistently outperforms existing approaches on two challenging benchmarks. In the future, we will address full rotational variations and deploy the proposed method on real drones for on-board localization.

## References

- [1] Sheng Ao, Qingyong Hu, Bo Yang, Andrew Markham, and Yulan Guo. Spinnet: Learning a general surface descriptor for 3d point cloud registration. In *CVPR*, pages 11753–11762, 2021. 2
- [2] Sheng Ao, Yulan Guo, Qingyong Hu, Bo Yang, Andrew Markham, and Zengping Chen. You only train once: Learning general and distinctive 3d local descriptors. *TPAMI*, 45(3):3949–3967, 2022. 2
- [3] Sheng Ao, Qingyong Hu, Hanyun Wang, Kai Xu, and Yulan Guo. Buffer: Balancing accuracy, efficiency, and generalizability in point cloud registration. In *CVPR*, pages 1255–1264, 2023. 2
- [4] Eduardo Arnold, Jamie Wynn, Sara Vicente, Guillermo Garcia-Hernando, Aron Monszpart, Victor Prisacariu, Daniyar Turmukhambetov, and Eric Brachmann. Map-free visual relocalization: Metric pose relative to a single image. In *ECCV*, pages 690–708. Springer, 2022. 2
- [5] Dan Barnes, Matthew Gadd, Paul Murcutt, Paul Newman, and Ingmar Posner. The oxford radar robotcar dataset: A radar extension to the oxford robotcar dataset. In *ICRA*, pages 6433–6438. IEEE, 2020. 6, 15
- [6] Paul J Besl and Neil D McKay. Method for registration of 3-d shapes. In *Sensor fusion IV: control paradigms and data structures*, pages 586–606. Spie, 1992. 6, 15
- [7] Eric Brachmann, Tommaso Cavallari, and Victor Adrian Prisacariu. Accelerated coordinate encoding: Learning to relocalize in minutes using rgb and poses. In *CVPR*, pages 5044–5053, 2023. 2
- [8] Samarth Brahmhatt, Jinwei Gu, Kihwan Kim, James Hays, and Jan Kautz. Geometry-aware learning of maps for camera localization. In *CVPR*, pages 2616–2625, 2018. 2
- [9] Holger Caesar, Varun Bankiti, Alex H Lang, Sourabh Vora, Venice Erin Liong, Qiang Xu, Anush Krishnan, Yu Pan, Giancarlo Baldan, and Oscar Beijbom. nusenes: A multimodal dataset for autonomous driving. In *CVPR*, pages 11621–11631, 2020. 2
- [10] Nicholas Carlevaris-Bianco, Arash K Ushani, and Ryan M Eustice. University of michigan north campus long-term vision and lidar dataset. *IJRR*, 35(9): 1023–1035, 2016. 6, 15
- [11] Xieyuanli Chen, Andres Milioto, Emanuele Palazzolo, Philippe Giguere, Jens Behley, and Cyrill Stachniss. Suma++: Efficient lidar-based semantic slam. In *IROS*, pages 4530–4537. IEEE, 2019. 2
- [12] Xiao Chen, Quanyi Li, Tai Wang, Tianfan Xue, and Jiangmiao Pang. Gennbv: Generalizable next-best-view policy for active 3d reconstruction. In *CVPR*, pages 16436–16445, 2024. 1
- [13] Florinel-Alin Croitoru, Vlad Hondru, Radu Tudor Ionescu, and Mubarak Shah. Diffusion models in vision: A survey. *TPAMI*, 45(9):10850–10869, 2023. 3
- [14] Aritra Dutta, Srijan Das, Jacob Nielsen, Rajat Subhra Chakraborty, and Mubarak Shah. Multiview aerial visual recognition (mavrec): Can multi-view improve aerial visual perception? In *CVPR*, pages 22678–22690, 2024. 1
- [15] Martin A Fischler and Robert C Bolles. Random sample consensus: a paradigm for model fitting with applications to image analysis and automated cartography. *Communications of the ACM*, 24(6):381–395, 1981. 4, 12
- [16] Andreas Geiger, Philip Lenz, Christoph Stiller, and Raquel Urtasun. Vision meets robotics: The kitti dataset. *IJRR*, 32(11):1231–1237, 2013. 6, 15
- [17] Peiyu Guan, Zhiqiang Cao, Junzhi Yu, Chao Zhou, and Min Tan. Scene coordinate regression network with global context-guided spatial feature transformation for visual relocalization. *RAL*, 6(3):5737–5744, 2021. 3
- [18] Jonathan Ho, Ajay Jain, and Pieter Abbeel. Denoising diffusion probabilistic models. *NeurIPS*, 33:6840–6851, 2020. 3
- [19] Yongshu Huang, Chen Liu, Minghang Zhu, Sheng Ao, Chenglu Wen, and Cheng Wang. Difflo: Semantic-aware lidar odometry with diffusion-based refinement. In *CVPR*, pages 17050–17059, 2025. 2
- [20] Zhaoyang Huang, Yan Xu, Jianping Shi, Xiaowei Zhou, Hujun Bao, and Guofeng Zhang. Prior guided dropout for robust visual localization in dynamic environments. In *ICCV*, pages 2791–2800, 2019. 3

- [21] Alex Kendall and Roberto Cipolla. Modelling uncertainty in deep learning for camera relocalization. In *ICRA*, pages 4762–4769. IEEE, 2016. 3
- [22] Giseop Kim, Sunwook Choi, and Ayoung Kim. Scan context++: Structural place recognition robust to rotation and lateral variations in urban environments. *IEEE TRO*, 38(3):1856–1874, 2021. 2
- [23] Diederik P Kingma and Jimmy Ba. Adam: A method for stochastic optimization. *arXiv preprint arXiv:1412.6980*, 2014. 7
- [24] Jacek Komorowski. Minkloc3d: Point cloud based large-scale place recognition. In *WACV*, pages 1790–1799, 2021. 3
- [25] Jacek Komorowski, Monika Wysoczanska, and Tomasz Trzcinski. Egonn: Egocentric neural network for point cloud based 6dof relocalization at the city scale. *RAL*, 7(2):722–729, 2021. 8, 16
- [26] Haotian Li, Yuying Zou, Nan Chen, Jiarong Lin, Xiyuan Liu, Wei Xu, Chunran Zheng, Rundong Li, Dongjiao He, Fanze Kong, et al. Mars-lvig dataset: A multi-sensor aerial robots slam dataset for lidar-visual-inertial-gnss fusion. *IJRR*, 43(8):1114–1127, 2024. 2, 7
- [27] Wen Li, Shangshu Yu, Cheng Wang, Guosheng Hu, Siqi Shen, and Chenglu Wen. Sgloc: Scene geometry encoding for outdoor lidar localization. In *CVPR*, pages 9286–9295, 2023. 3, 4, 7, 16
- [28] Wen Li, Yuyang Yang, Shangshu Yu, Guosheng Hu, Chenglu Wen, Ming Cheng, and Cheng Wang. Dif-floc: Diffusion model for outdoor lidar localization. In *CVPR*, pages 15045–15054, 2024. 3
- [29] Wen Li, Chen Liu, Shangshu Yu, Dunqiang Liu, Yin Zhou, Siqi Shen, Chenglu Wen, and Cheng Wang. Lightloc: Learning outdoor lidar localization at light speed. In *CVPR*, pages 6680–6689, 2025. 2, 7, 16
- [30] Zijun Li, Zhipeng Cai, Bochun Yang, Xuelun Shen, Siqi Shen, Xiaoliang Fan, Michael Paulitsch, and Cheng Wang. Condo: Continual domain expansion for absolute pose regression. In *AAAI*, pages 14628–14636, 2025. 3
- [31] Hyungtae Lim, Beomsoo Kim, Daebeom Kim, Eungchang Mason Lee, and Hyun Myung. Quatro++: Robust global registration exploiting ground segmentation for loop closing in lidar slam. *IJRR*, 43(5):685–715, 2024. 3
- [32] Dunqiang Liu, Shujun Huang, Wen Li, Siqi Shen, and Cheng Wang. Text to point cloud localization with multi-level negative contrastive learning. In *AAAI*, pages 5397–5405, 2025. 2
- [33] Jiuming Liu, Guangming Wang, Chaokang Jiang, Zhe Liu, and Hesheng Wang. Translo: A window-based masked point transformer framework for large-scale lidar odometry. In *AAAI*, pages 1683–1691, 2023. 2
- [34] Quan Liu, Hongzi Zhu, Zhenxi Wang, Yunsong Zhou, Shan Chang, and Minyi Guo. Extend your own correspondences: Unsupervised distant point cloud registration by progressive distance extension. In *CVPR*, pages 20816–20826, 2024. 3
- [35] Shubo Liu, Hongsheng Zhang, Yuankai Qi, Peng Wang, Yanning Zhang, and Qi Wu. Aerialvlm: Vision-and-language navigation for uavs. In *ICCV*, pages 15384–15394, 2023. 1
- [36] Lun Luo, Shuhang Zheng, Yixuan Li, Yongzhi Fan, Beinan Yu, Si-Yuan Cao, Junwei Li, and Hui-Liang Shen. Bevplace: Learning lidar-based place recognition using bird’s eye view images. In *ICCV*, pages 8700–8709, 2023. 2
- [37] Lun Luo, Si-Yuan Cao, Xiaorui Li, Jintao Xu, Rui Ai, Zhu Yu, and Xieyuanli Chen. Bevplace++: Fast, robust, and lightweight lidar global localization for unmanned ground vehicles. *IEEE TRO*, 41:4479–4498, 2025. 8, 16
- [38] Thien-Minh Nguyen, Shenghai Yuan, Muqing Cao, Yang Lyu, Thien Hoang Nguyen, and Lihua Xie. Ntu viral: A visual-inertial-ranging-lidar dataset, from an aerial vehicle viewpoint. *IJRR*, 41(3):270–280, 2022. 2, 6, 15
- [39] Yue Pan, Xingguang Zhong, Louis Wiesmann, Thorbjörn Posewsky, Jens Behley, and Cyrill Stachniss. Pin-slam: Lidar slam using a point-based implicit neural representation for achieving global map consistency. *IEEE TRO*, 40:4045–4064, 2024. 2
- [40] Charles Ruizhongtai Qi, Li Yi, Hao Su, and Leonidas J Guibas. Pointnet++: Deep hierarchical feature learning on point sets in a metric space. *NIPS*, 30, 2017. 2
- [41] Zheng Qin, Hao Yu, Changjian Wang, Yulan Guo, Yuxing Peng, and Kai Xu. Geometric transformer for fast and robust point cloud registration. In *CVPR*, pages 11143–11152, 2022. 3
- [42] Torsten Sattler, Qunjie Zhou, Marc Pollefeys, and Laura Leal-Taixe. Understanding the limitations of cnn-based absolute camera pose regression. In *CVPR*, pages 3302–3312, 2019. 3
- [43] Ruwen Schnabel, Roland Wahl, and Reinhard Klein. Efficient ransac for point-cloud shape detection. In *Computer graphics forum*, pages 214–226, 2007. 4
- [44] Tixiao Shan, Brendan Englot, Carlo Ratti, and Daniela Rus. Lvi-sam: Tightly-coupled lidar-visual-inertial odometry via smoothing and mapping. In *ICRA*, pages 5692–5698. IEEE, 2021. 2
- [45] Jamie Shotton, Ben Glocker, Christopher Zach, Shahram Izadi, Antonio Criminisi, and Andrew Fitzgibbon. Scene coordinate regression forests for camera relocalization in rgb-d images. In *CVPR*, pages 2930–2937, 2013. 3

- [46] Ravindu G Thalagala, Oscar De Silva, Awantha Jayasiri, Arthur Gubbels, George KI Mann, and Raymond G Gosine. Mun-fri: a visual-inertial-lidar dataset for aerial autonomous navigation and mapping. *IJRR*, 43(12):1853–1866, 2024. [6](#), [15](#)
- [47] Mikaela Angelina Uy and Gim Hee Lee. Pointnetvlad: Deep point cloud based retrieval for large-scale place recognition. In *CVPR*, pages 4470–4479, 2018. [3](#)
- [48] Guangming Wang, Xinrui Wu, Zhe Liu, and Hesheng Wang. Pwclo-net: Deep lidar odometry in 3d point clouds using hierarchical embedding mask optimization. In *CVPR*, pages 15910–15919, 2021. [2](#)
- [49] Sijie Wang, Qiyu Kang, Rui She, Wei Wang, Kai Zhao, Yang Song, and Wee Peng Tay. Hypilloc: Towards effective lidar pose regression with hyperbolic fusion. In *CVPR*, pages 5176–5185, 2023. [3](#)
- [50] Sijie Wang, Rui She, Qiyu Kang, Xingchao Jian, Kai Zhao, Yang Song, and Wee Peng Tay. Distilvpr: Cross-modal knowledge distillation for visual place recognition. In *AAAI*, pages 10377–10385, 2024. [2](#)
- [51] Sijie Wang, Siqi Li, Yawei Zhang, Shangshu Yu, Shenghai Yuan, Rui She, Quanjiang Guo, JinXuan Zheng, Ong Kang Howe, Leonrich Chandra, et al. Uavscenes: A multi-modal dataset for uavs. In *CVPR*, pages 28946–28958, 2025. [5](#), [6](#), [7](#), [15](#), [16](#)
- [52] Wei Wang, Bing Wang, Peijun Zhao, Changhao Chen, Ronald Clark, Bo Yang, Andrew Markham, and Niki Trigoni. Pointloc: Deep pose regressor for lidar point cloud localization. *IEEE Sensors Journal*, 22(1):959–968, 2021. [3](#)
- [53] Xiaoyang Wu, Li Jiang, Peng-Shuai Wang, Zhijian Liu, Xihui Liu, Yu Qiao, Wanli Ouyang, Tong He, and Hengshuang Zhao. Point transformer v3: Simpler faster stronger. In *CVPR*, pages 4840–4851, 2024. [4](#), [8](#)
- [54] Zhenyu Wu, Karthik Suresh, Priya Narayanan, Hongyu Xu, Heesung Kwon, and Zhangyang Wang. Delving into robust object detection from unmanned aerial vehicles: A deep nuisance disentanglement approach. In *ICCV*, pages 1201–1210, 2019. [1](#)
- [55] Yan Xia, Yusheng Xu, Shuang Li, Rui Wang, Juan Du, Daniel Cremers, and Uwe Stilla. Soe-net: A self-attention and orientation encoding network for point cloud based place recognition. In *CVPR*, pages 11348–11357, 2021. [2](#)
- [56] Yan Xia, Mariia Gladkova, Rui Wang, Qianyun Li, Uwe Stilla, Joao F Henriques, and Daniel Cremers. Casspr: Cross attention single scan place recognition. In *ICCV*, pages 8461–8472, 2023. [2](#), [3](#)
- [57] Bochun Yang, Zijun Li, Wen Li, Zhipeng Cai, Chenglu Wen, Yu Zang, Matthias Muller, and Cheng Wang. Lisa: Lidar localization with semantic awareness. In *CVPR*, pages 15271–15280, 2024. [2](#), [3](#)
- [58] Fan Yang, Lin Guo, Zhi Chen, and Wenbing Tao. One-inlier is first: Towards efficient position encoding for point cloud registration. In *NIPS*, pages 6982–6995, 2022. [3](#)
- [59] Yuyang Yang, Wen Li, Sheng Ao, Qingshan Xu, Shangshu Yu, Yu Guo, Yin Zhou, Siqi Shen, and Cheng Wang. Raloc: Enhancing outdoor lidar localization via rotation awareness. In *ICCV*, pages 3304–3313, 2025. [2](#), [3](#), [4](#), [7](#), [16](#)
- [60] Huan Yin, Xuecheng Xu, Sha Lu, Xieyuanli Chen, Rong Xiong, Shaojie Shen, Cyrill Stachniss, and Yue Wang. A survey on global lidar localization: Challenges, advances and open problems. *IJCV*, 132(8): 3139–3171, 2024. [2](#)
- [61] Shangshu Yu, Cheng Wang, Yitai Lin, Chenglu Wen, Ming Cheng, and Guosheng Hu. Stcloc: Deep lidar localization with spatio-temporal constraints. *TITS*, 24(1):489–500, 2022. [2](#)
- [62] Chongjian Yuan, Jiarong Lin, Zuhao Zou, Xiaoping Hong, and Fu Zhang. Std: Stable triangle descriptor for 3d place recognition. In *ICRA*, pages 1897–1903, 2023. [3](#)
- [63] Dongkun Zhang, Jiaming Liang, Ke Guo, Sha Lu, Qi Wang, Rong Xiong, Zhenwei Miao, and Yue Wang. Carplanner: Consistent auto-regressive trajectory planning for large-scale reinforcement learning in autonomous driving. In *CVPR*, pages 17239–17248, 2025. [2](#)
- [64] Ethan Zhang and Neda Masoud. Increasing gps localization accuracy with reinforcement learning. *TITS*, 22(5):2615–2626, 2020. [2](#)
- [65] Ji Zhang, Sanjiv Singh, et al. Loam: Lidar odometry and mapping in real-time. In *RSS*, pages 1–9. Berkeley, CA, 2014. [2](#)
- [66] Tongzhou Zhang, Gang Wang, Yu Chen, Hai Zhang, and Jue Hu. Multi-constellation-inspired single-shot global lidar localization. In *AAAI*, pages 10404–10412, 2024. [2](#)
- [67] Lei Zhou, Zixin Luo, Tianwei Shen, Jiahui Zhang, Mingmin Zhen, Yao Yao, Tian Fang, and Long Quan. Kfnet: Learning temporal camera relocalization using kalman filtering. In *CVPR*, pages 4919–4928, 2020. [3](#)

# Beyond Ground: Map-Free LiDAR Relocalization for UAVs

## Supplementary Material

In this document, we present supplementary material, including the implementation of MAILS, details of the UAVLoc dataset, and additional experimental results and analyses to complement the main paper. Section 6 provides a detailed implementation of MAILS, including its parameter settings, complexity analysis and the invariant encoding. Section 7 presents details and visualizations of our UAVLoc dataset, and in Section 8, we report additional experimental results on the UAVLoc\_U dataset. We further present visualizations and analyses of failure cases in Section 9. Finally, Section 10 outlines potential directions for future work.

## 6. MAILS Details

### 6.1. Parameter Settings

In this section, we provide detailed parameter settings for MAILS, as illustrated in Fig. 8. In the preprocessing stage, we set the voxel size to 0.3 m and the pooling kernel size of the downsampling layer to  $k = 2$ . In the Feature Initialization module, we configure the feature dimension of the Softmax-free LoSWAtt module to 64, the number of attention heads to 2, and the sliding-window size to 8. Subsequently, we use three Feature Encoding modules (i.e.,  $M = 3$ ) to further encode the features. For each module, we set the pooling kernel size to  $k = 2$ , the number of LoSWAtt blocks to  $N = [2, 2, 4]$ , the feature dimensions to 128, 256, and 512, the numbers of attention heads to 4, 8, and 16, and the sliding-window sizes to 8, 8, and 16. Finally, we employ six MLP layers (i.e.,  $T = 6$ ), each with 1024 units, to regress the output coordinates. Detailed procedures are provided in Algorithm 1. For the final pose estimation, we apply RANSAC [15] with an inlier threshold of 0.6 m. We use all point-wise correspondences and enforce geometric consistency through edge-length (0.9) and distance-based checks. The RANSAC procedure runs with a maximum of 100,000 iterations and a confidence of 0.999.

### 6.2. Complexity Analysis

A standard self-attention layer over  $n$  points requires computing all pairwise interactions, resulting in a quadratic complexity of  $O(n^2C)$ , which is prohibitive for UAV LiDAR frames where  $n$  often exceeds 10K. Our LoSWAtt module exploits the spatial continuity introduced by space-filling-curve ordering and restricts attention to a local sliding window. For each point, we attend only to its  $k$  preceding and  $k$  following points along the ordered sequence, forming a window of size  $2k+1$ . Consequently, each query token is involved in at most  $2k+1$  attention computations,

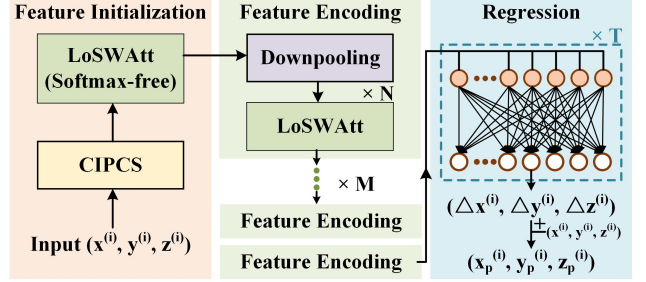


Figure 8. The parameter settings of MAILS, where  $N = [2, 2, 4]$ ,  $M = 3$ ,  $T = 6$ .

---

### Algorithm 1 MAILS

---

**Require:** Query point cloud  $\mathbf{P}_t \in \mathbb{R}^{N \times 3}$   
**Ensure:** Estimated UAV pose  $p^*$

- 1: **Step 1: CIPCS**
- 2: **for**  $i = 1$  to  $N$  **do**
- 3:    $\mathbf{f}_i = \varphi(C)$
- 4: **end for**
- 5:  $\mathbf{F}_{\text{seq}} = \text{Serialize}(\text{Downsample}(\{\mathbf{f}_i\}))$
- 6: **Step 2: LoSWAtt**
- 7: **for**  $i = 1$  to  $N$  **do**
- 8:   SW:  $s_i = \max(1, i - k) : \min(N, i + k)$
- 9:    $F_i^w = \{\mathbf{f}_j \mid j \in s_i\}$
- 10:    $r_j = \mathbf{p}_j - \mathbf{p}_i, \theta_j = \text{pitch}(\mathbf{p}_j), j \in s_i$
- 11:    $\mathbf{Q}, \mathbf{K}, \mathbf{V} = P_{Q,K,V}(F_i^w)$ ,
- 12:    $\mathbf{Q}_2 = \varphi_2(\mathbf{f}_i)$
- 13:    $K_2 = \varphi_3[(r_j, \theta_j) \mid j \in s_i]$
- 14:   **if**  $i == 1$  **then**
- 15:      $\mathbf{f}'_i = (\frac{\mathbf{Q}\mathbf{K}^\top}{\sqrt{D}} + \frac{\mathbf{Q}_2\mathbf{K}_2^\top}{\sqrt{D_2}})\mathbf{V}$
- 16:   **else**
- 17:      $\mathbf{f}'_i = \text{Softmax}(\frac{\mathbf{Q}\mathbf{K}^\top}{\sqrt{D}} + \frac{\mathbf{Q}_2\mathbf{K}_2^\top}{\sqrt{D_2}})\mathbf{V}$
- 18:   **end if**
- 19: **end for**
- 20:  $\mathbf{F}' = \{\mathbf{f}'_i\}_{i=1}^N$
- 21: **Step 3: Coordinate Regression**
- 22:  $\mathbf{Y}' = \{\text{MLP}_{\text{reg}}(\mathbf{f}'_i)\}_{i=1}^N$
- 23: **Step 4: Pose Estimation**
- 24:  $p^* = \arg \min_{T_p \in \mathbb{R}^{4 \times 4}} \sum_{i=1}^M \|T_p \mathbf{P}_t^{(i)} - \mathbf{y}'_i\|_2$
- 25: **Step 5: Training Loss**
- 26:  $\mathcal{L}_{L1} = \frac{1}{|\mathbf{P}_t|} \sum_i \|\mathbf{y}'_i - \mathbf{y}_i^*\|_1$
- 27: **return**  $p^*$

---

and the computational complexity becomes:

$$O((2k+1)nC),$$

which is linear in  $n$  and significantly more scalable than global attention. This yields an effective reduction factor of approximately  $n/(2k+1)$  in the number of pairwise interactions. Meanwhile, the locality constraint introduced by the sliding window further preserves geometric structure, enabling the model to capture yaw- and altitude-invariant features.

### 6.3. Invariant Encoding

To analyze the invariance properties of MAILs, we adopt a token-level description that eliminates dependence on absolute yaw and altitude. We first define the local geometric token, which is used to construct the positional-bias term  $K_2$  in LoSWAtt.

**Definition 1** (Local Geometric Token). *For each sliding window centered at index  $i$ , the local geometric token is*

$$G_i = \{(r_j, \theta_j)\}_{j=i-k}^{i+k} \in \mathbb{R}^{(2k+1) \times 2},$$

where

$$r_j = \|p_j - p_i\|_{xy}, \quad \theta_j = \arctan\left(\frac{z_j - z_i}{\|p_j - p_i\|_{xy}}\right),$$

and  $p_i$  denotes the raw 3D coordinates. By construction,  $G_i$  depends only on local relative geometry, and thus the positional-bias term  $K_2$  derived from  $G_i$  is invariant under yaw rotations and altitude shifts.

**Definition 2** (Invariant Feature Initialization). *Let  $F_i^w$  denote the features extracted from CIPCS and serialized within the sliding window around  $i$ . Applying a constant linear transformation  $M$  (e.g., MLP weights) yields features*

$$F_i^w = CM,$$

which are independent of absolute coordinates and yaw-altitude transformations.

**Proposition 1** (Yaw-Altitude Invariance of LoSWAtt). *For the LoSWAtt output at position  $i$ ,*

$$f'_i = \text{Softmax}\left(\frac{QK^\top}{\sqrt{D}} + \frac{Q_2K_2^\top}{\sqrt{D_2}}\right)V,$$

we have

$$\Psi(R \circ F_i^w, R \circ G_i) = \Psi(F_i^w, G_i), \quad \forall R \in SO(2) \times \mathbb{R}.$$

*Proof.* From Definition 1 and 2, the inputs satisfy

$$R \circ F_i^w = F_i^w, \quad R \circ G_i = G_i.$$

LoSWAtt contains:

1. content term  $QK^\top$  depending only on  $F_i^w$ ,
2. positional-bias term  $Q_2K_2^\top$  depending only on  $G_i$ .



Figure 9. Data collection platform of UAVLoc.

Both remain unchanged under  $R$ , and since  $V$  is linear  $F_i^w$ , the output  $f'_i$  is invariant.

**Theorem 1** (Local Yaw-Altitude Invariance of MAILs). *For the full encoder  $\Phi(P_t)$  (CIPCS + LoSWAtt), and any  $R \in SO(2) \times \mathbb{R}$ ,*

$$\Phi(R \circ P_t) = \Phi(P_t).$$

*Proof.* Each output  $f'_i$  is invariant by Proposition 1:

$$\begin{aligned} f'_i &= \text{Softmax}\left(\frac{QK^\top}{\sqrt{D}} + \frac{Q_2K_2^\top}{\sqrt{D_2}}\right)V \\ &= \text{Softmax}\left(\frac{Q_RK_R^\top}{\sqrt{D_R}} + \frac{Q_{R2}K_{R2}^\top}{\sqrt{D_{R2}}}\right)V_R \\ &= f'_{Ri}. \end{aligned}$$

where the contributions of both the content term  $QK$  and the positional-bias term  $Q_2K_2^\top$  are preserved, which shows that the full encoder  $\Phi(P_t)$  is yaw-altitude invariant.

## 7. UAVLoc Details

Here, we provide additional details of the UAVLoc dataset, and a summary is presented in Tab. 5. UAVLoc exhibits several distinctive characteristics that make it challenging and representative for UAV relocalization: 1) Multiple flight paths. 2) Irregular flight paths. 3) Altitude variation.

### 7.1. Data Collection Platform

The data collection platform of UAVLoc is illustrated in Fig. 9. All sensors are mounted on a DJI M300 RTK industrial UAV. The primary perception sensors include a PSDK 102 V3 camera and an Ouster OS1-128 LiDAR, which are synchronized using a hardware time-synchronization module. The on-board computer is used to control the UAV and collect the raw LiDAR point cloud data.

Table 5. **Summary of UAVLoc’s sequences and their characteristics.** Laboratory belongs to UAVLoc\_C, School, Town, and Road belong to UAVLoc\_U.

Scene names	Sequence	LiDAR Frames	Duration (s)	Altitude Range (m)	Size ( $km^2$ )	Scenarios & Characters
Laboratory	Laboratory_1	5.9k	330	45 - 47	~0.7	laboratory park
	Laboratory_2	8.0k	561	54 - 60		laboratory park (Ascent altitude)
	Laboratory_3	7.2k	415	48 - 50		laboratory park
	Laboratory_4	10.7k	568	43 - 45		laboratory park (Reduce altitude)
School	School_1	7.0k	351	78 - 83	~1.8	school area
	School_2	8.3k	416	79 - 82		school area
	School_3	7.2k	410	83 - 87		school area (Ascent altitude)
Town	Town_1	9.3k	475	74 - 80	~1.0	rural towns
	Town_2	10.7k	535	76 - 82		rural towns
	Town_3	10.7k	535	80 - 85		rural towns (Ascent altitude)
Road	Road_1	8.7k	453	70 - 76	~1.7	Interchanges & Highways
	Road_2	9.4k	472	71 - 74		Interchanges & Highways
	Road_3	9.8k	490	75 - 80		Interchanges & Highways (Ascent altitude)
Total/Average		112.9k/8.7k	6011/462	40 - 90	5.2/1.3	-

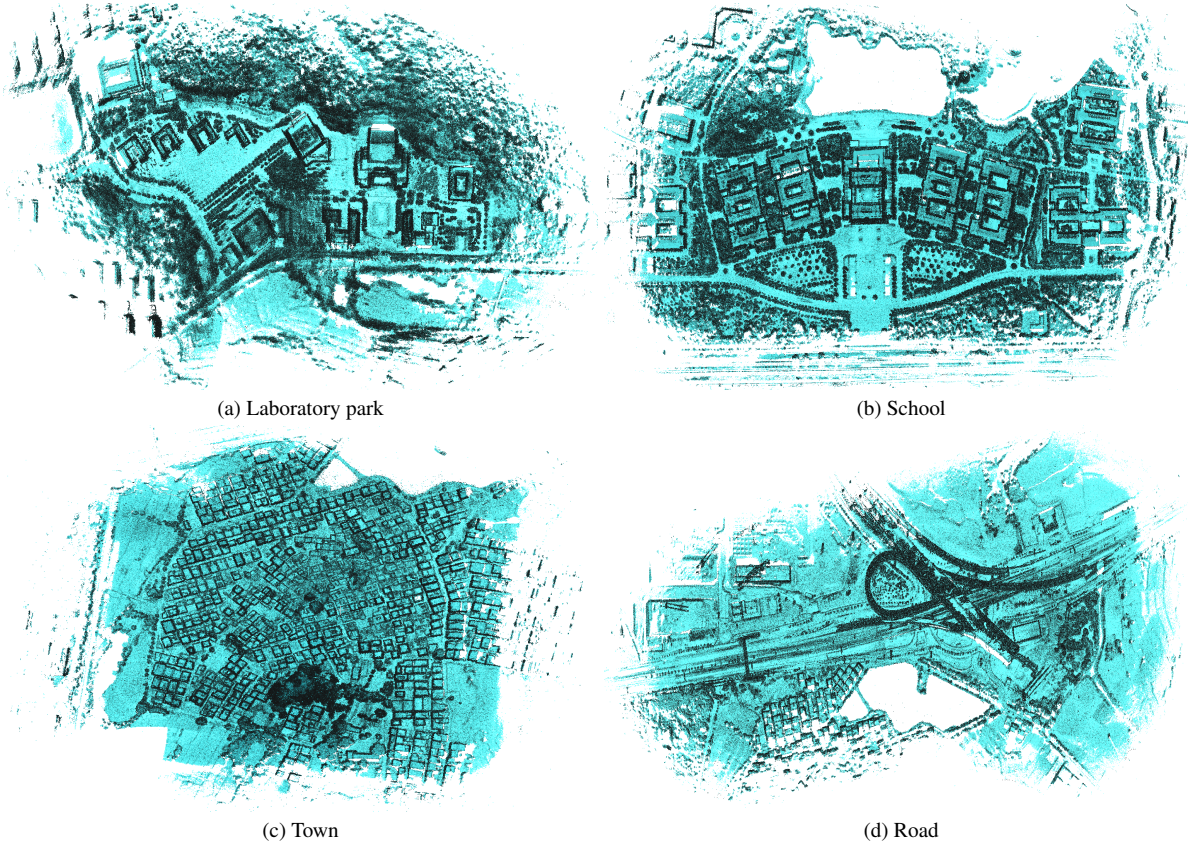


Figure 10. **Visualization of scene maps.** We used ground truths to reconstruct scene maps, demonstrating the accuracy of our ground truth.

Table 6. **Results on UAVLoc\_U dataset.** We report the mean error [m/°] for six methods on the UAVLoc\_U datasets.

Method	Map-based Relocalization		Map-free Relocalization				
	BEVPlace++	Egonn	SGLoc	SGLoc+RA	LightLoc	RALoc	ours
School_3	156.82m,39.88°	45.91m,24.27°	94.19m,49.90°	72.97m,49.90°	47.96m,37.41°	41.05m,34.76°	<b>14.31m,19.36°</b>
Town_3	43.54m,11.50°	11.78m,8.75°	15.53m,9.99°	15.52m,9.98°	2.48m,1.62°	9.52m,3.00°	<b>1.52m,1.48°</b>
Road_3	45.68m,11.92°	13.33m,10.57°	27.17m,11.10°	24.20m,22.70°	16.22m,15.79°	26.03m,15.14°	<b>3.80m,2.92°</b>
Average	82.01m,21.10°	23.67m,14.53°	45.63m,23.67°	37.56m,27.53°	22.22m,18.28°	25.53m,17.63°	<b>6.54m,7.92°</b>

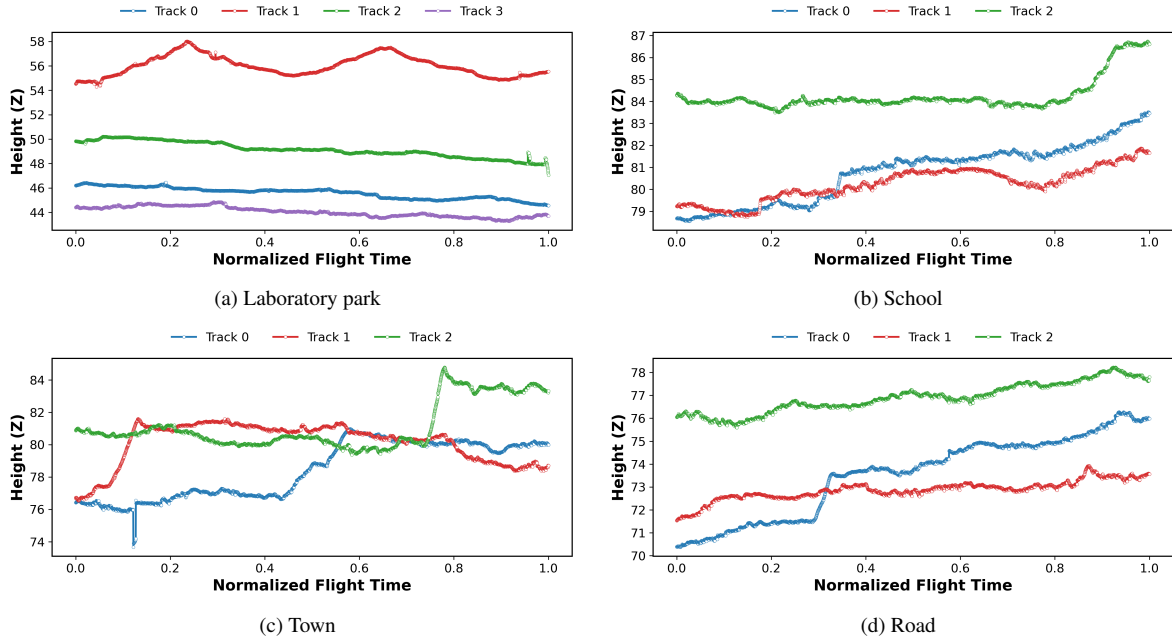


Figure 11. **Visualization of flight altitudes along different trajectories.** Normalized flight time: scales the flight duration of each trajectory to a common baseline of 1.

## 7.2. Ground Truth Pose

In UAVLoc, we use only the LiDAR point clouds for relocalization. The camera data are processed with DJI Terra to obtain high-precision UAV poses, which are then aligned with the LiDAR frames through camera calibration and time synchronization. Moreover, due to inevitable UAV vibrations during flight, we further refine the LiDAR poses by performing ICP [6] between each LiDAR frame and the high-precision point cloud map generated by DJI Terra, yielding highly accurate LiDAR poses. This process enables us to derive an accurate 6-DoF ground-truth pose for every LiDAR scan.

To validate the accuracy of the ground truth, we reconstructed global maps for four scenes using the obtained poses. As shown in Fig. 10, the reconstructed maps demonstrate the high accuracy of our ground truth. Collectively, these results confirm the stability and reliability of our pose estimation pipeline across various environments.

## 7.3. Irregular Flight Paths

UAVLoc includes multiple flights for each scene. Unlike existing datasets such as UAVScenes [51], each flight in UAVLoc follows a unique and non-repetitive trajectory. As a result, the LiDAR scans from different flights share only partial spatial overlap with the training data, making the relocalization task significantly more challenging. Furthermore, in UAVLoc\_U, the higher flight altitude places the LiDAR near its effective sensing range and reduces the field

of view, further decreasing the overlap between scans.

## 7.4. Altitude Variation

Unlike existing relocalization datasets, UAVLoc explicitly accounts for the impact of altitude variations during UAV flight on relocalization performance. As illustrated in Figure 11, altitude variations in UAVLoc manifest in two primary aspects: (1) Smooth altitude changes during flight. Due to factors such as air turbulence, UAVs continuously make small altitude corrections during operation. The collected UAVLoc data realistically captures and reflects this natural flight behavior. (2) In real-world operations, UAVs often operate across a wide range of altitudes. Unlike existing datasets such as UAVScenes, which maintain fixed flight altitudes, UAVLoc offers a more realistic benchmark for evaluating under varying altitude conditions.

## 7.5. Compared with other datasets

Compared to ground vehicle datasets [5, 10, 16], UAVLoc is collected using UAV platforms, resulting in more complex and irregular flight trajectories and more frequent, pronounced altitude variations. NTU-VIRAL [38] includes random UAV trajectories and altitude variations within the same scenes, making it usable for relocalization tasks. However, its relatively short flight paths limit comprehensive and reliable evaluation of relocalization performance. In contrast, while MUN-FRL [46] provides large-scale UAV flight data, each scene contains only a single trajectory, making it unsuitable for relocalization research.

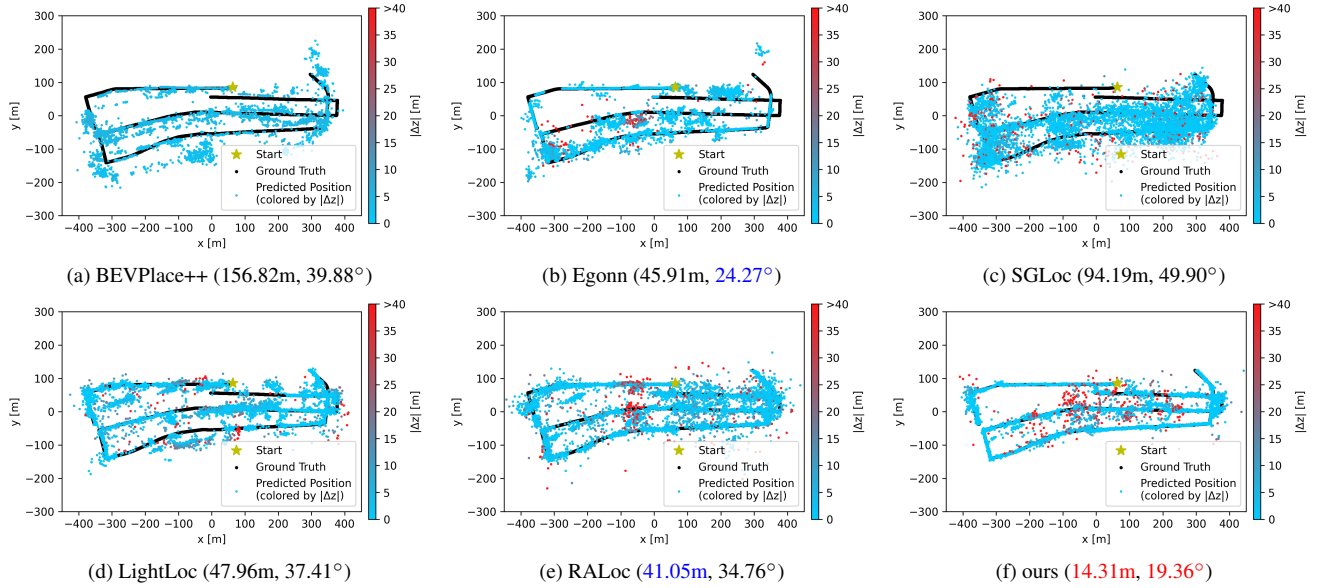


Figure 12. Localization results of different methods on the UAVLoc\_U dataset (School\_3). We highlight the **best** and **second-best** results.

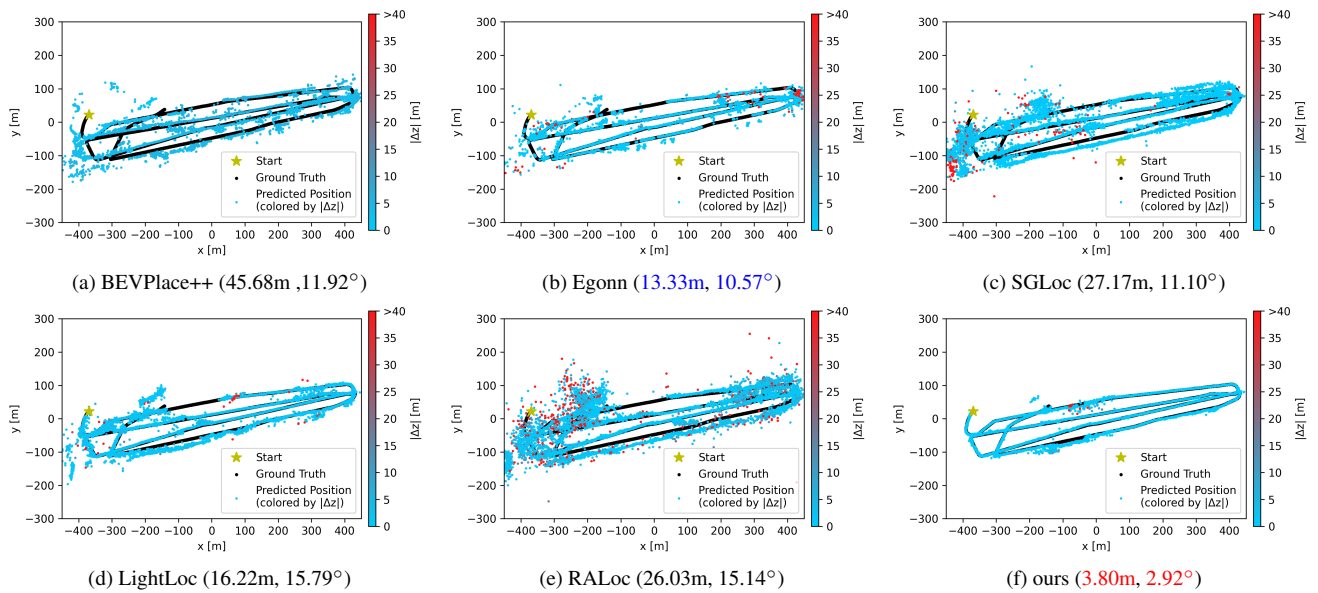


Figure 13. Localization results of different methods on the UAVLoc\_U dataset (Road\_3). We highlight the **best** and **second-best** results.

UAVScenes [51] is among the few large-scale UAV LiDAR datasets for relocalization. However, the multiple trajectories within each scene largely follow identical routes and altitudes, failing to reflect the diverse flight behaviors of real-world UAV operations. To address these limitations, UAVLoc provides flight data that better reflects real-world UAV operations, with irregular trajectories and variable altitudes, making it suitable for evaluating UAV relocalization models.

## 8. Additional Experiments on UAVLoc\_U

Here, we report the results of BEVPlace++ [37], Egonn [25], SGLoc [27], SGLoc+RA [27], LightLoc [29], RALoc [59] and our MAILS on the UAVLoc\_U dataset. As shown in Tab. 6, the relatively high-altitude flights introduce additional challenges for UAV relocalization, particularly in the School scene. Most methods—especially the map-free ones—show a clear increase in both position and orientation errors compared with their performance on UAVLoc\_U. De-

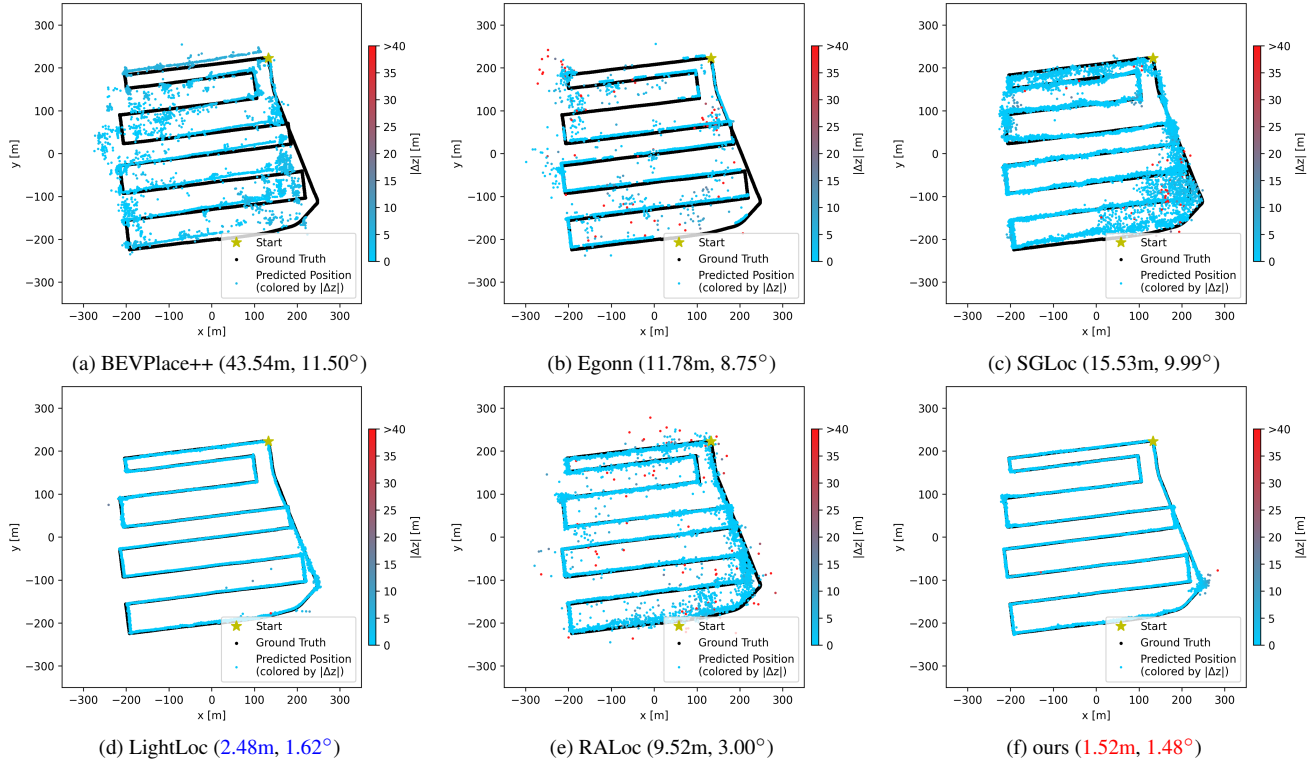


Figure 14. Localization results of different methods on the UAVLoc\_U dataset (Town\_3). We highlight the **best** and **second-best** results.

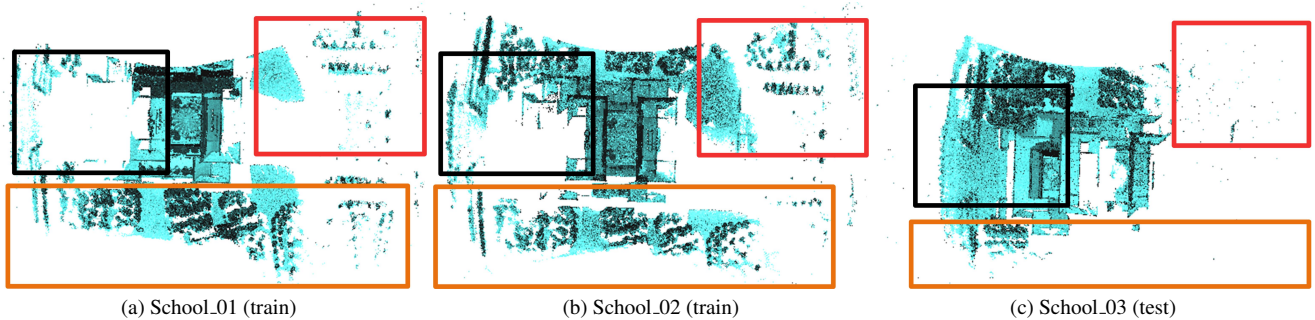


Figure 15. **Failure Case on UAVLoc\_U (School)**. Changes in altitude and rotation lead to alterations in the receptive field. In the test set, due to the increased flight altitude, a denser and more complete high-plane point cloud (roof) was obtained, while the low-plane point cloud became sparse and reduced in coverage (ground).

spite this, our method still achieves state-of-the-art accuracy with an average error of 6.54m and 7.92°. BEVPlace++ exhibits limited adaptability to UAV viewpoints; although its orientation accuracy (21.10°) is competitive, its reliance on BEV-style priors results in a 82.01m average position error. Egonn further exposes this limitation, suffering dramatic performance degradation (23.67m, 14.53°) due to its inability to handle significant UAV pose changes. Among map-free baselines, SGLoc and SGLoc+RA perform moderately but remain sensitive to yaw and altitude variations. Rotation augmentation provides some improvement

(SGLoc+RA reduces position/orientation error by 8.07m and 3.85°, yet its effect is inconsistent; School\_3 still yields a high 49.90° orientation error. LightLoc achieves strong results on Town\_3 (2.48m, 1.62°) but lacks mechanisms to model UAV-specific 3D pose diversity, leading to poor overall generalization (22.22 m, 18.28°). RALoc shows the strongest robustness among existing methods, but still produces a relatively large average position error (25.53m).

Across all scenes, our method consistently outperforms all baselines by a substantial margin, demonstrating strong resilience to UAV-specific viewpoint, yaw, and altitude vari-

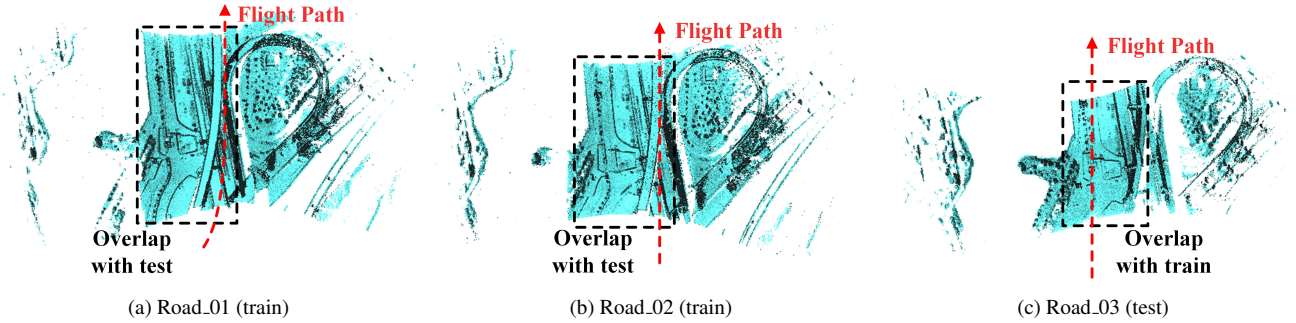


Figure 16. **Failure Case on UAVLoc\_U (Road)**. The irregular flight paths result in fewer overlapping areas. Due to the irregular flight paths, when the test set appears relatively distant from the training set, it results in smaller overlapping regions, thereby leading to a decline in relocalization accuracy.

ations. Furthermore, to more comprehensively demonstrate methods’ performances, the experimental visualization results on UAVLoc\_U are presented in Figs. 12, 13, and 14.

## 9. Failure Case

In UAVLoc\_U, nearly all methods exhibited localization errors significantly higher than in other scenarios. Although our MAILS achieves significantly better performance than other methods, it also exhibits substantial errors on a small subset of test data. We consider the primary reasons for these failure cases to be the following two points: (1) Changes in altitude and rotation lead to alterations in the receptive field, which is shown in Fig. 15. (2) The irregular flight paths result in fewer overlapping areas, which is shown in Fig. 16.

As shown in Fig. 15, we provide visualizations of scans from sections where the model exhibited poor test-set performance. As shown, variations in UAV flight altitude and rotational transformations lead to substantial differences in the LiDAR field of view between test-time scans and those seen during training—even when captured at the same physical location. These discrepancies, particularly around structures such as rooftops and doorways, result in significantly reduced overlap between training and test data. Consequently, these sections show notably higher relocalization errors.

Additionally, as shown in Fig. 16, we also visualized the trajectory segments that deviated on Road\_3. The reason for the relatively large prediction error in this segment is due to the limited overlap between the test set and the training set. In this case, the UAV deviated significantly to the left during testing compared to its training flight path, resulting in the loss of most structured information on the right side. The only overlapping area was the central roadway. Similarly, smaller overlapping areas resulted in reduced positioning accuracy.

## 10. Future Work

The above analysis of failure cases has revealed the limitations that currently exist in our MAILS. To address these limitations, in future works, we will proceed along several research directions.

First, we plan to incorporate altitude- and rotation-robust geometric priors into the feature extraction pipeline. While our current design introduces partial invariance through space-filling curve ordering and windowed attention, stronger geometric normalization mechanisms—such as learned canonicalization or viewpoint-adaptive tokenization—may further reduce discrepancies caused by large viewpoint shifts.

Second, we aim to improve robustness under limited or asymmetric spatial overlap, which frequently occurs in practical UAV deployments. A promising direction is to integrate cross-sequence global context modeling, enabling the network to infer scene-level structural consistency even when local observations are partially missing.

Finally, since UAV flight behavior inherently exhibits variability, we will explore self-supervised pretraining strategies that expose the model to a wider distribution of viewpoints, altitudes, and motion patterns. Such pretraining may allow MAILS to generalize beyond the specific trajectories seen during supervised training.

Overall, we believe these directions can further strengthen the robustness and generalization capability of MAILS, bringing it closer to practical UAV relocalization in diverse, unconstrained environments.